Phase sensitivity of the pair-creation process in colliding laser pulses

C. K. Li,[1] Y. J. Li,[1] Q. Su,[2] and R. Grobe[2]
[1]*State Key Laboratory for GeoMechanics and Deep Underground Engineering, China University of Mining and Technology, Beijing 100083, China*
[2]*Intense Laser Physics Theory Unit and Department of Physics, Illinois State University, Normal, Illinois 61790-4560, USA*

(Received 5 June 2023; accepted 22 August 2023; published 25 September 2023)

We examine the electron-positron pair-creation process from the quantum vacuum triggered by two colliding laser beams in the presence of a nuclear binding potential. Once the two pulses overlap, they form a standing-wave pattern with nodes or antinodes in the region where the nucleus is placed. As the resulting spatial intensity pattern depends on the phase between both fields, it can be used to control the pair-creation yield. It turns out that the ground-state capture of the created electrons can actually be largest for those laser phases that lead to nodes (dark intensity regions) where the nucleus is located and not for those that lead to antinodes (bright intensity regions). Furthermore, this phase can be used to control selectively into which excited state the created electrons are predominately captured.

DOI: 10.1103/PhysRevA.108.033112

I. INTRODUCTION

The quantum vacuum state is a fundamental concept in quantum field theory referring to the lowest energy state [1,2]. This state is actually highly dynamic and has numerous interesting features, such as, vacuum fluctuations where particle-antiparticle pairs continuously pop in and out of existence due to the inherent uncertainty of quantum mechanics. The concept of the vacuum plays a crucial role in the renormalization process of quantum field theory [3], which is a technique used to handle infinite or divergent quantities in calculations of quantum field theories. It is also central to the Casimir effect [4–7], where quantum vacuum fluctuations between closely spaced conductive plates lead to attractive or even repulsive force between the plates. The most relevant feature in the present work is the phenomenon that excitations of the quantum vacuum can lead to particle creation and annihilation processes, especially in high-energy or intense electromagnetic fields [8,9]. These processes play a significant role in various physical phenomena, such as pair production in strong electric fields or Hawking radiation near black holes [10]. An understanding of the properties and behavior of the quantum vacuum is essential in many areas of theoretical and experimental physics, ranging from quantum electrodynamics to the study of particle physics and cosmology [11].

Traditionally, there have been at least two major ways of probing the vacuum's properties. In the first one, the strong external field was generated by the superposition of two Coulombic fields as characteristic of ultrarelativistic collision of two highly charged nuclei [12–16]. Here during the short crossing time of the two nuclei, the sum of the nuclear charge numbers can exceed 173, which for an extended nucleus with a finite radius leads to a supercritical field (137 for a point nucleus). This supercritical field can then break down the vacuum state, leading to the creation of an electron-positron pair. The theoretical as well as experimental interest in these processes was spurred in the past few decades by the relativistic heavy-ion facilities AGS (Alternating Gradient Synchrotron) and RHIC (Relativistic Heavy Ion Collider) at Brookhaven, and SPS (Super Proton Synchrotron) and LHC (Large Hadron Collider) at CERN. Of central importance to all of these investigations is the Sauter-Schwinger effect [17–19], where a spatially homogeneous static electric field generates electron-positron pairs from the vacuum state. Many theoretical and computational studies have focused on the electrostatic situation in which a supercritical field (such as that provided by highly charged nuclei) can create particles pairs [20–22].

In the second way of probing the vacuum's properties, the excitations were provided by electromagnetic fields [23–26]. While it is well known that independent of its strength, a single plane-wave field itself is not capable of breaking down the vacuum, there are several electromagnetic or even electrostatic field configurations under which the pair-creation process can become possible. Due to the promising development of new laser systems with very high power, several theoretical studies have focused on examining the vacuum's breakdown process triggered by two or several mutually colliding laser beams. Since the early pioneering multiphoton-induced pair-creation experiments at the Stanford Linear Accelerator Center (SLAC) in 1994 [27], several worldwide laboratories, such as the Extreme-Light Infrastructure [28], the Center for Relativistic Laser Science [29], the SLAC [30], the Rutherford Appleton Laboratory [31], and the European X-Ray Free-Electron Laser [32], have been exploring new means to probe the quantum vacuum with very intense electromagnetic radiation fields. In most theoretical studies, the spatial dependence of the laser beams was often neglected, and the fields were approximated by periodically oscillatory electric field pulses [33]. Early perturbative analytical studies of this simplified geometry go back to the 1970s [34–38]. There have also been many interesting studies in which the space-time structures of the optimum field

configuration that maximizes the created particle yield were explored [39–43].

In addition to probing the vacuum state solely with either static Coulomb fields or electromagnetic radiation, effective combinations of both environments have also been explored [44,45]. In fact, laser-assisted electron-positron pair generation using a nucleus provides numerous additional parameters to control the dynamics, including the possibility of exploiting resonances. Therefore, resonant processes are excellent candidates for probing the predictions of QED in the presence of a strong external field. Although there have been several investigations [46–51] that were devoted to these laser-nucleus configurations, a complete description of this problem is still a challenge, and the resonant situation in particular is far from complete. The resonant laser-assisted Bethe-Heitler process [52] for the case of a weak monochromatic [53,54] and pulsed [55,56] plane-wave field was also examined.

In the present work, we explore a simple model system to probe the quantum vacuum state using both the presence of a highly charged nucleus as well as two colliding electromagnetic fields. We examine an interesting regime in which neither the nucleus by itself nor the two colliding laser fields are sufficient to create electron-positron pairs. In a recent study [57], the impact of a highly charged nucleus in the focal region of two mutually colliding laser pulses was studied computationally for a simple model system. Here the possibility of the subsequent capture of the created electrons by the nucleus dynamically enhanced the final particle yield. It was predicted that the mutual phase relationship between the two laser beams can have a pivotal impact on the pair-creation process.

In this work, we examine these spatiotemporal effects from a broader perspective by focusing on the relationship between the length scales provided by the spatial inhomogeneity of the laser, and the extension of the lowest-lying bound states of the nucleus. For situations in which the nucleus is centered in a node of the two lasers' standing-wave pattern, it is counterintuitively predicted that the pair creation can be larger than for a configuration where the nucleus is placed at a low-intensity node instead of the high-intensity antinode. The dynamics is also modeled phenomenologically to allow us to vary its characteristic parameters.

The manuscript is structured as follows. In Sec. II we review our methodology of computational quantum field theory and introduce the model system for the nucleus with its energy level structure. In the absence of the nucleus, the laser-vacuum interaction is characterized by a reversible single-beam Volkov-like mechanism as well as a two-beam dressing mechanism. In Sec. III we show how the pair-creation process can be controlled by the phase between both beams. Here the relationship between the nuclear extension and the lasers' wavelength leads to qualitatively different responses of the vacuum. In Sec. IV we track the origin of the counterintuitive phase dependence of the ground-state capture rate to the behavior of a single transition matrix element. In Sec. V we derive an analytical expression for the interlaser phase dependence of the pair-creation rate. In Sec. VI our main findings are generalized to the multiphoton pair-creation process. We complete this article with an outlook on further challenges in Sec. VII.

II. MODEL SYSTEM FOR THE NUCLEUS AND THE FIELD CONFIGURATION

In Sec. II A, we will briefly review first our particular approach based on computational quantum field theory to model the pair-creation process. In Sec. II B we describe the model of the two colliding laser beams, and in Sec. II C we show the difference between the fully reversible single- and two-beam dressing of the vacuum state. In Sec. II D we discuss the energy level structure introduced to the dynamics by a model nuclear field.

A. Numerical quantum field theory

In the framework of computational quantum field theory (CQFT) [58], all dynamical features of the pair-creation process are provided by the electron-positron field operator Ψ, whose space-time evolution is governed by the Dirac equation $i\hbar\partial\Psi/\partial t = H\Psi$. Here the usual Hamiltonian in one spatial dimension is given by

$$H = c\sigma_1[p - eA(z,t)/c] + mc^2\sigma_3 + eV(z), \tag{2.1}$$

where $A(z,t)$ models the external electromagnetic fields, $V(z)$ is the binding potential of the nucleus, σ_1 and σ_3 are the two 2×2 Pauli matrices, e is the positive amount of the electron's charge, m is the electron's mass, and c is the speed of light. The (single-particle) energy eigenstates of the Hamiltonian $H_0 \equiv c\sigma_1 p + mc^2\sigma_3 + eV(z)$ in the absence of the space-time-dependent field $A(z,t)$, defined by $H_0|\alpha\rangle = E_\alpha|\alpha\rangle$, can be partitioned according to their energy into three groups. If $E_\alpha \geqslant mc^2$, we denote these positive continuum energy states as $|p\rangle$; if their energy is inside the mass gap, $-mc^2 < E_\alpha < mc^2$, we denote these discrete electronic bound states as $|i\rangle$; and if their energy $E_\alpha \leqslant -mc^2$ is part of the negative energy continuum, we denote these states as $|n\rangle$. If we introduce the sets of (anticommuting) creation operators $(B_p^\dagger, B_i^\dagger, D_n^\dagger)$ and corresponding annihilation operators (B_p, B_i, D_n) associated with these particular states, the mode expansion of the quantum field operator is given by

$$\begin{aligned}\Psi(t) &= \Sigma_p B_p(t)|p\rangle + \Sigma_i B_i(t)|i\rangle + \Sigma_n D_n^\dagger(t)|n\rangle \\ &= \Sigma_p B_p|p(t)\rangle + \Sigma_i B_i|i(t)\rangle + \Sigma_n D_n^\dagger|n(t)\rangle,\end{aligned} \tag{2.2}$$

where $|\alpha(t)\rangle$ is the single-particle solution to $i\hbar\partial|\alpha(t)\rangle/\partial t = H|\alpha(t)\rangle$ with the initial state $|\alpha(t=0)\rangle = |\alpha\rangle$.

We note that this particular mode expansion is different from the traditional CQFT approach [13,58], where one usually uses field-free eigenstates of H_0 with $V = 0$, labeled by their (conserved) momentum. In this easier case, the corresponding observables can be interpreted as the true quantities after *both* A and V are turned off abruptly in time [59–66]. If we use the orthogonality among the dressed eigenstates $|\alpha\rangle$, we can derive the time evolution of the operators as

$$B_p(t) = \Sigma_{p'} B_{p'}\langle p|p'(t)\rangle + \Sigma_i B_i\langle p|i(t)\rangle + \Sigma_n D_n^\dagger\langle p|n(t)\rangle, \tag{2.3a}$$

$$B_i(t) = \Sigma_{p'} B_{p'}\langle i|p'(t)\rangle + \Sigma_{i'} B_{i'}\langle i|i'(t)\rangle + \Sigma_n D_n^\dagger\langle i|n(t)\rangle, \tag{2.3b}$$

$$D_n^\dagger(t) = \Sigma_{p'} B_{p'}\langle n|p'(t)\rangle + \Sigma_i B_i\langle n|i(t)\rangle + \Sigma_{n'} D_{n'}^\dagger\langle n|n'(t)\rangle. \tag{2.3c}$$

The set of all matrix elements $U_{\alpha',\alpha}(t) \equiv \langle \alpha'|\alpha(t)\rangle$ of the unitary time evolution operator are the basic building blocks of computational quantum field theory.

The initial quantum field theoretical state is given here by the vacuum $|\Phi(t=0)\rangle = |\mathrm{VAC}\rangle$. Here $|\mathrm{VAC}\rangle$ denotes the vacuum state in the *presence* of the nucleus, defined as $B_p|\mathrm{VAC}\rangle = B_i|\mathrm{VAC}\rangle = D_n|\mathrm{VAC}\rangle = 0$.

As a side remark, we note that traditionally, the vacuum is described in the Dirac sea picture with a completely filled continuum of states with negative energy. If an external field is capable of transferring this population through the band gap of energy $2mc^2$, this is interpreted as the creation of electron-positron pairs. In our situation, due to the presence of the potential, there are also electronic bound states within this gap, which can also help the depletion process from the lower continuum.

The total number of electrons $N(e^-,t)$ and positrons $N(e^+,t)$ follow from the quantum field theoretical expectation values

$$N(e^-,t) \equiv \langle \Phi(t=0)|\Sigma_p B_p^\dagger(t)B_p(t) + \Sigma_i B_i^\dagger(t)B_i(t)|\Phi(t=0)\rangle, \tag{2.4a}$$

$$N(e^+,t) \equiv \langle \Phi(t=0)|\Sigma_n D_n^\dagger(t)D_n(t)|\Phi(t=0)\rangle, \tag{2.4b}$$

where we consistently have $N(e^-,t) = N(e^+,t) \equiv N(t)$ as the result of the total charge conservation. If we insert the specific initial state $|\Phi(t=0)\rangle = |\mathrm{VAC}\rangle$ into these expressions and use the solutions Eqs. (2.3), we obtain $N(e^-,t) = \Sigma_p\Sigma_n|U_{p,n}(t)|^2 + \Sigma_i\Sigma_n|U_{i,n}(t)|^2$. This shows that for computational purposes, only the set of negative energy continuum states $|n\rangle$ needs to be evolved. This set is the generalization of the usual Dirac sea, but it includes here the important impact of the nuclear field on these states. In fact, several of the phase-based effects discussed below occur only as a result of these crucial modifications to the usual Dirac sea by the potential $V(z)$.

The introduction of a time-dependent particle number during the interaction is certainly a nontrivial issue, and numerous very recent [64–66] and also older works [59–63] have been devoted to this important topic. In the context of our computational quantum field theory, the electron-positron field operator is the central quantity. To obtain the true observable density of physical positrons (electrons) at a given time t, one must project this operator onto the corresponding submanifold of instantaneous energy eigenstates associated with positrons (electrons) at that moment in time. This is challenging due to the inherent energy degeneracy of supercritical systems.

In several works, the force-free energy eigenstates of the Dirac Hamiltonian are used as a basis to expand the field operator [analogous to our Eq. (2.2)]. In this case, the resulting time-dependent number of created particles has the following meaning. It corresponds precisely to the true physical number of particles only if all external fields were turned off simultaneously at that time. As the (unavoidable) time dependence of (even an abrupt) turn-off shape of the potential triggers additional pair annihilation and creation processes, this particular quantity describes (contains) both the true particles during the interaction as well as the particles that *would be* created or annihilated associated solely with a sudden turn-off process of the field to zero.

As we take the static potential fully into account in our expansion Eq. (2.2), we have to interpret the $N(e^-,t)$ and $N(e^+,t)$ [defined in Eqs. (2.4)] as the true particle number if the laser field is turned off abruptly at that time. As the fields themselves are turned off smoothly in our dynamics [see Eqs. (2.5)], $N(e^-,t)$ and $N(e^+,t)$ naturally become the true particle after the interaction.

B. Electromagnetic field configuration and the vacuum's dynamical response

In general, the characteristic spatial and temporal scales for the electron-positron dynamics are naturally provided by the fermions' Compton wavelength $\lambda \equiv \hbar/(mc) = 3.8\times10^{-13}$ m and the time $T \equiv \hbar/(mc^2) = 1.3\times10^{-21}$ s. The corresponding scales associated with the laser are its wavelength $\lambda_L = 2\pi/k$ and its optical period $T_L \equiv 2\pi/\omega$, which are related to the speed of light $c = \lambda_L/T_L$. To simulate the space-time profile of the two ultrashort laser fields, we chose for the left and right traveling vector potentials the form

$$A_r(z,t) \equiv f(t)A_0 S(z-ct+z_0)\sin(\omega t - kz + \alpha), \tag{2.5a}$$

$$A_l(z,t) \equiv f(t)A_0 S(z+ct-z_0)\sin(\omega t + kz). \tag{2.5b}$$

As a consequence of the (1+1)-dimensional nature of our model quantum field theory, the polarization direction is in the z-direction. To approximately characterize the basic space-time features of each laser beam, we chose its spatial shape as $S(z) \equiv \{\tanh[(z+d_L)/w_L] - \tanh[(z-d_L)/w_L]\}/2$ with a total extension of about $2d_L$. As the spatial ramp up and down distance w_L is chosen much less than d_L, this pulse resembles almost a rectangular profile, which simplifies the interpretation of the pair creation and also the laser dressing data computed below. The two beams are initially centered at $\pm z_0$. As their initial spacing $2z_0$ was chosen much larger than their extension $2d_L$, initially the two pulses do not overlap in space.

Similar to the spatial profile, the temporal shape is also characterized by three temporal domains. Its turn-on for $0 \leqslant t/T_L \leqslant 5$ is given as $f(t) = \sin^2[\pi t/(10T_L)]$, which is then followed by a constant plateau region $5 \leqslant t/T_L \leqslant 20$ with $f(t) = 1$. Finally, for $20 \leqslant t/T_L \leqslant 25$, the field is turned off, $f(t) = \cos^2[\pi(t-20T_L)/(10T_L)]$. As the beams enter and leave the interaction zone close to $z = 0$ due to their propagation properties, there is no immediate computational or physical necessity for having our beams turned on and off in time. However, the inclusion of $f(t)$ helps us to better understand the occurrence of the field-induced dressing of the vacuum, as discussed below.

We choose for our total electromagnetic field configuration the superposition $A(z,t;\alpha) \equiv A_r(z,t) + A_l(z,t)$.

As is customary in many theoretical investigations, this field configuration with a plateau region was chosen for interpretational convenience. Due to the purely temporal turn-on represented by $f(t)$, it does not satisfy the (vacuum) Maxwell equations. Also, the transverse nature of a true electromagnetic field in three dimensions cannot be represented due to

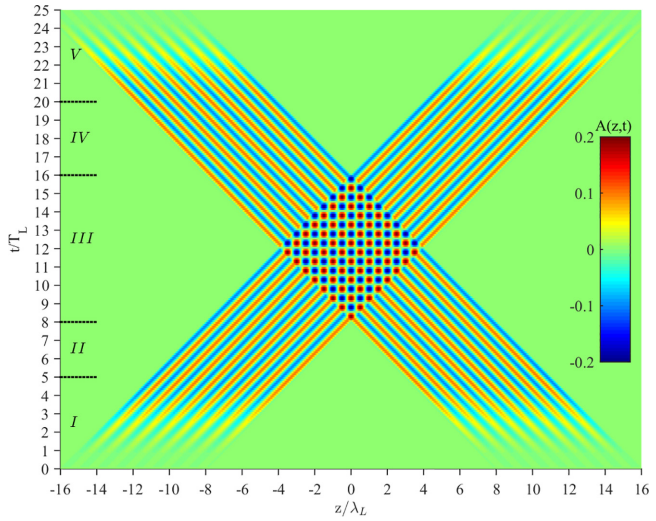

FIG. 1. Space-time resolved contour plot of the total electric field associated with the two colliding field pulses of frequency $\omega = 0.5\,\mathrm{mc}^2/\hbar$. The spatial parameters in units of the wavelength $\lambda_L = 4\pi\lambda = 12.56\lambda$ are $z_0 = 12\lambda_L$, $d_L = 4\lambda_L = 50.24\lambda$, $w_L = 0.1\lambda = 0.007\,962\lambda_L$, and $\alpha = 0$, leading to an antinode at $z = 0$ when both pulses cross. Initially, the pulses are centered at $z_0 = \pm 12\lambda_L$ and turned on and off over $5T_L$.

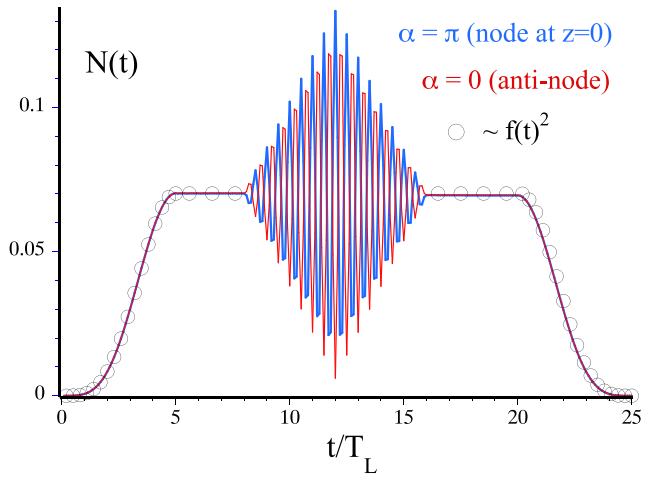

FIG. 2. The time dependence number of electron-positron pairs $N(e^-, t)$ during the interaction of the two colliding laser pulses graphed in Fig. 1. The parameters in our numerical simulations are the same as in Fig. 1.

the spatial constraint of the dynamics, and there is no magnetic field.

To better visualize the total field, we have displayed its contour plot in Fig. 1 inside our numerical box of total length $L = 32\lambda_L$ extending from $z = -16\lambda_L$ to $16\lambda_L$. The particular choice for our field configuration leads to five different temporal regions. The first and last regimes (I and V) are characterized by the sine-squared-like temporal turn-on and -off over five cycles. In region II ($5 \leqslant t/T_L \leqslant 8$) the two fully established pulses propagate shape invariant towards each other. At a time approximately equal to $t = (z_0 - d_L)/c = 8T_L$, the two wave fronts of the beams meet at $z = 0$, which enter the overlap region III. Here they form a standing-wave pattern with an antinode $A(z,t) \sim \sin(\omega t)\cos(kz)$ for the interpulse phase difference $\alpha = 0$ and with a node $A(z,t) \sim \cos(\omega t)\sin(kz)$ for $\alpha = \pi$. During this dynamically most important region, the spatial overlap grows from zero [for time $(z_0 - d_L)/c = 8T_L$] to a maximum of time $t = (z_0 + d_L)/c = 12T_L$ and then decreases back to zero at time $(z_0 + 2d_L)/c = 16T_L$. In region IV ($16 \leqslant t/T_L \leqslant 20$), the two pulses no longer overlap and move away from each other until they are turned off in region V ($20 \leqslant t/T_L \leqslant 25$).

C. Single-beam Volkov dressing and two-beam dressing of the vacuum

For a better comparison with the dynamical role of the nucleus, we study here first the pair-creation process in the absence of any nuclear field, $V = 0$. This will help us to estimate the role and the characteristics of a temporary dressing due to the sole laser-vacuum interaction for our parameters.

In Fig. 2 we graph the number of electron-positron pairs $N(t) = \Sigma_i \langle B_i^\dagger(t) B_i(t)\rangle + \Sigma_p \langle B_p^\dagger(t) B_p(t)\rangle$ as a function of time. $N(t)$ grows during the temporal turn-on region I ($0 < t < 5T_L$). As the match with the superimposed open circles [proportional to $f(t)^2$] in the figure shows, $N(t)$ is proportional to the square of the instantaneous envelope of $A(t)$. It is characterized first by the adiabatic transition into the single-beam Volkov regime II, where $N(t)$ becomes constant after $t = 5T_L$.

This amount is directly proportional to the spatial extension of the laser pulse. This nonoscillatory regime II, which can be modeled by the exact Volkov solution for a single plane-wave field [67–70] associated with $H = c\sigma_1[p - eA_r(z,t)/c] + mc^2\sigma_3$, is then followed by a qualitatively different oscillatory dressing regime III, associated with the standing-wave region ($8T_L < t < 16T_L$), when both fields overlap. The nearly triangular envelope with maximum $N(t)$ at $t = 12T_L$ is characteristic of the resulting overlap area of two nearly rectangular pulses that are moving through each other. It also suggests that this particular two-beam dressing is fully reversible. After the interaction, the final populations $N(t = 25T_L) = 6.45 \times 10^{-6}$ for the antinode ($\alpha = 0$) configuration, and $N(t = 25T_L) = 6.03 \times 10^{-6}$ for node ($\alpha = \pi$), are both very small, which suggests that the chosen field strengths $A_0 = 0.1\,\mathrm{mc}^2/e$ were too small to generate any permanent particle pairs.

We note that in this case the two negligible final yields display also a very weak dependence on the phase α. To further investigate, we conducted additional simulations for significantly stronger fields, where the pair-creation process is no longer negligible. Upon increasing the original field strength $A_0 = 0.1\,\mathrm{mc}^2/e$ by a factor of 10, the final yield increased by almost six orders of magnitude. This is consistent with the expected increase of the continuum-continuum transitions and the irreversible creation of real particles beyond just dressing. On the other hand, the disparity between the two configurations for $\alpha = 0$ and $\alpha = \pi$ remained consistently less than 3%, suggesting that in this case any nodal or antinodal pattern at $z = 0$ is indeed irrelevant.

In contrast, below we will see that once the potential $V(z)$ is included, these fully reversible single- (Volkov-like) and

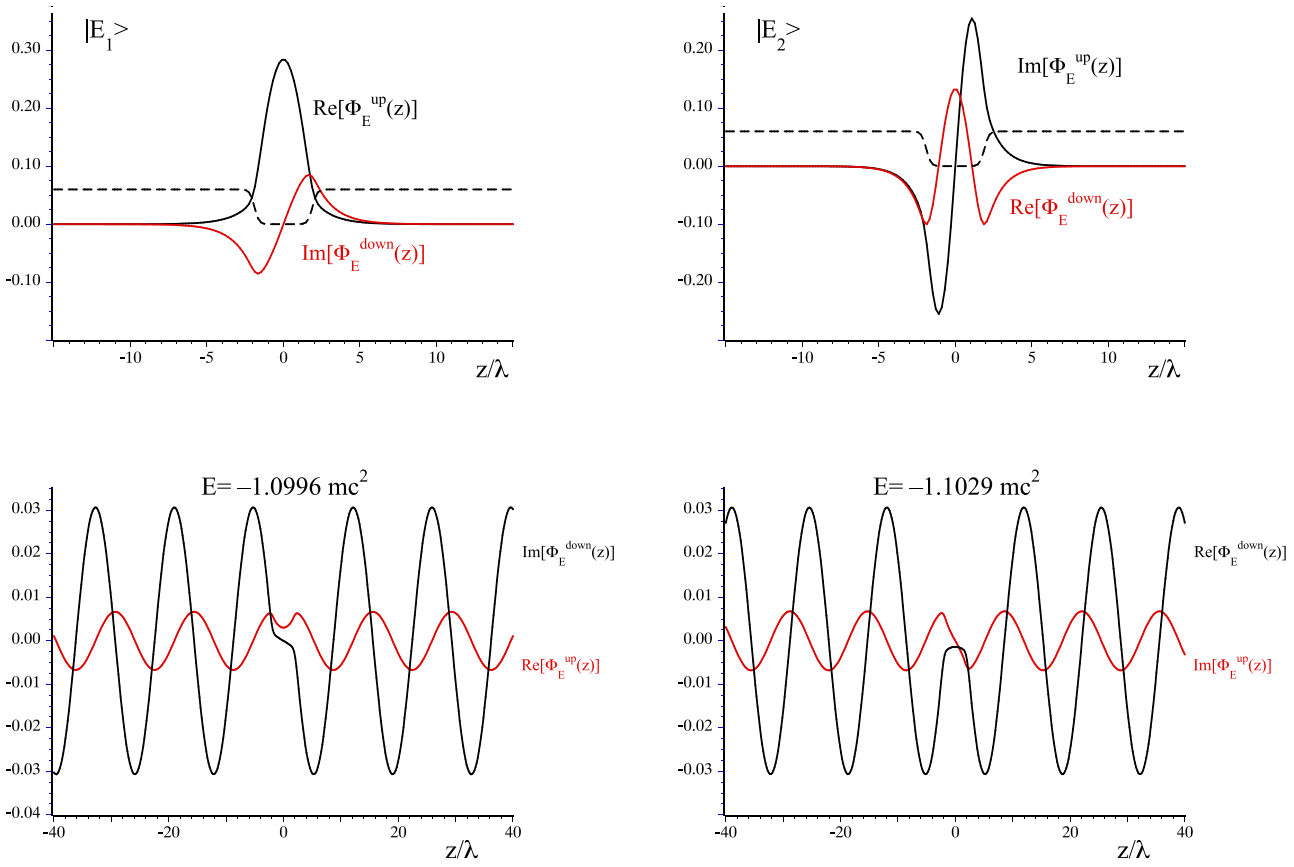

FIG. 3. The spatial structure (in units of the Compton wavelength λ) of the spinor components of the ground state $|E_1\rangle$, the first excited state $|E_2\rangle$, and two dressed negative continuum states $|E\rangle$ with negative and positive parity for energy close to $-1.1\,\mathrm{mc}^2$. For comparison, to indicate the spatial scale relevant for the laser interaction, we also graph the scaled and uplifted shape of the nuclear potential modeled as $V(z) = V_0\{\tanh((z+d)/w) - \tanh((z-d)/w)\}/2$, with $V_0 = -1.85\,\mathrm{mc}^2$, $d = 1.95\lambda$, and $w = 0.3\lambda$. The states $|E\rangle$ were obtained by numerical diagonalization of the Dirac Hamiltonian $c\,\sigma_1\,p + mc^2\,\sigma_3 + eV(z)$ in a box of size $L = 32\lambda_L = 401.92\lambda$.

double-beam dressing structures [71] will be superimposed by the irreversible creation of real particles.

D. Nuclear model potential and its energy structure

To simulate the dynamical impact of a binding field, we introduce the spatially localized scalar potential $V(z)$ in the Dirac Eq. (2.1). It is characterized by an extension d, and its spatial dependence is modeled as $V(z) = V_0\{\tanh((z+d)/w) - \tanh((z-d)/w)\}/2$, as sketched by the dashed line in Fig. 3. For the specific parameters, given by the strength $V_0 = -1.85\,\mathrm{mc}^2$, spatial extension $2d = 3.9\lambda$, and ramp width $w = 0.3\lambda$, it supports four electronic bound states of energies $E_1 = -0.6\,\mathrm{mc}^2$, $E_2 = -0.1\,\mathrm{mc}^2$, $E_3 = 0.45\,\mathrm{mc}^2$, and $E_4 = 0.92\,\mathrm{mc}^2$.

As the potential was chosen spatially symmetric, i.e., $V(z) = V(-z)$, the Dirac Hamiltonian H_0 commutes with a generalized (relativistic) parity operator P, given by the product of the spatial inversion and complex conjugation operators. This symmetry has its manifestation for the spatial dependence of the upper and lower spinors $\{\Phi_E^{\mathrm{up}}(z),\ \Phi_E^{\mathrm{down}}(z)\}$ of all energy eigenstates of H_0. This means that for parity (+), all corresponding energy eigenstates $|E^{(+)}\rangle$ can be chosen with an upper spinor component that is even in space and real $\{\Phi_E^{\mathrm{up}}(z) = \Phi_E^{\mathrm{up}}(-z)$ and $\Phi_E^{\mathrm{up}}(z) = \Phi_E^{\mathrm{up}}(z)^*\}$, while the lower spin component is imaginary and odd. Similarly, the (–) parity states $|E^{(-)}\rangle$ can be chosen with an odd and real upper component and an imaginary and even lower spinor component. This is illustrated in Fig. 3, where we show the spatial dependence of the two spinor components of the ground-state and first excited-state wave functions.

For a laser frequency of $\omega = 0.5\,\mathrm{mc}^2/\hbar$, the lower Dirac state with energy $E_c = E_1 - \hbar\omega = -1.1\,\mathrm{mc}^2$ can couple resonantly to the ground state via the absorption of a single photon. As the spatial profile of the (initially populated) continuum state is crucially important for our analysis below, we also show two neighboring energy states with even and odd parity in the figure. These wave functions with energies $E = -1.0996$ and $-1.1029\,\mathrm{mc}^2$ were obtained by numerical diagonalization of the Hamiltonian in its discretized spatial representation in a finite box.

As might be expected, the continuum states $|E^{(\pm)}\rangle$ outside the nuclear region ($|z| > 2d$) are periodic. However, we note that the state has a characteristic "hole" close to the origin $z = 0$, where the nucleus is located. For comparison, the undressed states $|e^{(\pm)}\rangle$ [associated with the Hamiltonian $c\sigma_1 p + mc^2\sigma_3$, but not shown in the figure] are entirely periodic in z [28]. In

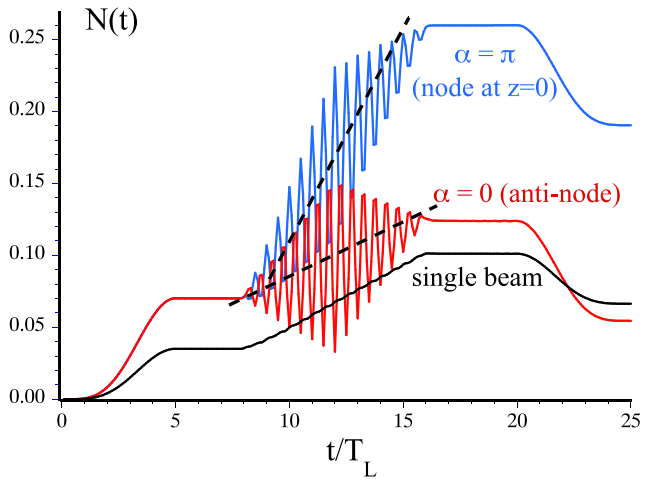

FIG. 4. The time dependence of the total number of created electrons and positrons $N(t)$. The nonoscillatory black curve is due to the interaction with a single pulse. The other two graphs are for the two crossing laser pulses with mutual phase difference $\alpha = 0$, leading to an antinode at $z = 0$, and $\alpha = \pi$, leading to a node at $z = 0$. The parameters of the two pulses [Eq. (1)] (with amplitude $A_0 = 0.1\,\mathrm{mc}^2/e$, $\hbar\omega = 0.5\,\mathrm{mc}^2$) are the same as in Fig. 1. The parameters of the potential ($V_0 = -1.85\,\mathrm{mc}^2$, $d = 1.95\lambda$, and $w = 0.3\lambda$) are the same as in Fig. 3. We have included by the two straight dashed lines the predicted slopes obtained from Sec. V.

fact, the dressing due to the nucleus acts in two ways. First, the probability density close to $z = 0$ is suppressed leading to the hole, and second, the waves outside the potential regions are shifted inwards or outwards depending on the parity (required by wave-function continuity around the edges of the nuclear potential). This local dressing due to the nucleus is quite relevant for the interaction with the two laser fields, as we will show in Sec. V below.

III. PAIR-CREATION PROCESS INDUCED BY TWO COLLIDING LASER FIELDS

In this section, we will examine the effect of the laser phase α, the relationship between the lasers' wavelength, and the spatial extension of the nucleus with regard to the final pair-creation yield. We will see that its phase dependence can be completely reversed, depending on these spatial scales.

A. Smaller laser frequency ω and small nuclear potential extension d

To determine the dynamical role of the nuclear potential $V(z)$ on the pair creation, we have graphed in Fig. 4 the time dependence of the number of electron-positron pairs $N_{\mathrm{single}}(t)$ created solely by the single right-traveling field $A(z,t) = A_r(z,t)$. In addition to the temporary dressing nature already discussed in Fig. 2, the shape of region III is now characterized by a nonreversible quasilinear growth. As a result, we have a nonzero number of permanently created pairs $N(t = 25T_L) = 0.0664$ after the interaction. The numerically obtained pair-creation rate (slope) of $N_{\mathrm{single}}(t)$ in this quasilinear growth regime III amounts in atomic units to $dN_{\mathrm{single}}/dt = 12.3$. We have repeated the simulation for different laser phases α and found no significant impact as one might have expected as the second field $A_l(z,t)$ was not present in this simulation.

To include the dynamical impact of the second counterpropagating field, we have repeated our simulation using both beams, $A(z,t) = A_r(z,t) + A_l(z,t)$. In the two Volkov dressing regions I and II, we find that the monotonous growth is exactly twice that of the single field, $N(t) = 2N_{\mathrm{single}}(t)$, which is expected as both pulses do not overlap yet and dress the vacuum at different locations in space, as discussed above in Fig. 2.

However, once we enter the two-pulse overlap region III, the vacuum's response to the two pulses is qualitatively different due to the presence of the nucleus (compared to Fig. 2). Here the oscillatory two-beam dressing is superimposed by a linear growth, whose slope clearly depends on α. For a phase $\alpha = 0$, leading to an antinode of the standing waves at $z = 0$, the effective slope $dN/dt = 10.2$ is actually about 17% less than the single-field slope dN_{single}/dt, which reads off the graph as 12.3. As a result of this rather unexpected reduction, the final population amounts here only to $N(t = 25T_L) = 0.0545$. This means that the introduction of the second (counterpropagating) field $A_l(z,t)$ surprisingly *decreases* the pair-creation yield.

Even more remarkable, for the other extreme choice of the phase $\alpha = \pi$, for which the two fields form a (low-intensity) node around $z = 0$, the pair-creation yield is actually *enhanced*. Here the effective slope in region III amounts to the slope $dN/dt = 35.06$, which exceeds single-field slope dN_{single}/dt by 185.07%. The resulting final number of created pairs is $N(t = 25T_L) = 0.1905$.

This observed phase dependence of the final yield (at time T) is completely counterintuitive and opposite to what one would have expected. It surprisingly predicts that for the configuration ($\alpha = \pi$), where the two crossing fields form a *node* close to the nucleus, i.e., a region of basically *vanishing* electrical field intensity, the particle yield $N_{\mathrm{tot}}(T, \alpha = \pi)$ is almost four times *larger* compared to the (antinode) field configuration for $\alpha = 0$, where the laser intensity close to $z = 0$ is maximum. By analyzing the coupling elements in Sec. IV, we will suggest that this surprise is actually a direct manifestation of the nucleus-induced deformation (hole) of the negative energy states, as we showed in Fig. 3.

B. Using the phase α to control the electron capture into selected bound states

To examine this unexpected observation, we have repeated our simulations for the entire range of phase α between 0 and π. In Fig. 5 we show the final number of created particle pairs $N(T)$ at the final time $T = 25T_L$ as a function of the phase α, allowing us to scan systematically and continuously through the node/antinode regimes. We find that the total number of created pairs is indeed largest if the two fields form a node ($\alpha = \pi$) at $z = 0$, and it is unexpectedly smallest for $\alpha = 0$ when the intensity is largest at the region around $z = 0$.

To examine the dynamical role of each individual bound state into which the created electrons can be captured, we have

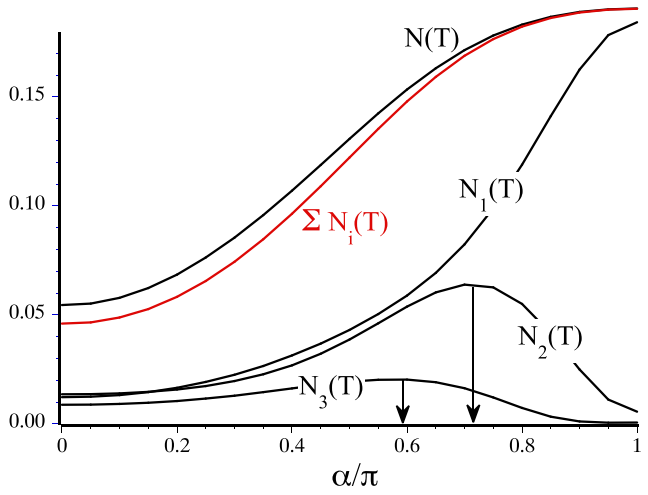

FIG. 5. The final number of created electrons (at $T = 25T_L$) as a function of the interlaser beams' phase α. The curve $N(T)$ is the total number of pairs, whereas $N_i(T)$ is the captured portion in the bound state $|E_i\rangle$. The red curve $\Sigma_{i=1}^4 N_i(T)$ is the total number of those electrons that were captured by the nucleus. The arrows mark the optimal phases to maximize the yield in a particular bound state. The other parameters for the nucleus and the laser beams are the same as in Fig. 4.

graphed in the figure the final occupation number $N_i(T)$ in the lowest three bound states. We find that the ground-state population $N_1(T)$ qualitatively mirrors the final total yield with larger differences for smaller angle α. As one might expect based on the energetic considerations, the single-photon coupled ground state's capture yield is largest, $N_1(T) = 0.184$ ($\alpha = \pi$) and $0.0123(\alpha = 0)$, amounting to nearly 22.5% and 96.7% of all created electrons for $\alpha = 0$ and $\alpha = \pi$, respectively.

Quite interestingly, the captured occupation in the first excited state $N_2(T)$ is qualitatively different. In Fig. 3 we have shown the double-peaked structure of its spatial probability $|\Phi_{E_2}^{\rm up}(z)|^2 + |\Phi_{E_2}^{\rm down}(z)|^2$. The yield $N_2(T)$ takes its maximum at an intermediate value of the phase $\alpha_{\rm max} = 0.7\pi$, where the field forms neither a node nor an antinode at $z = 0$. In fact, here the node (antinode) is located at $z = 0.07\lambda_L(-0.18\lambda_L, 0.32\lambda_L)$, respectively.

Similarly, if we want to maximize the capture rate into the second excited state $N_3(T)$, we have to choose a smaller phase $\alpha_{\rm max} = 0.6\pi$. This shows that the phase α can be used as an externally controllable means not only to maximize the overall total yield, but even to determine selectively into which excited state the created electrons are predominately captured.

We have also included in the figure the sum of all four bound-state probabilities $\Sigma_{i=1}^4 N_i(T)$. This shows that for phases close to $\alpha = \pi$, most of the created electrons are indeed captured by the potential $V(z)$. More interesting, however, is the observation that for small phases α, the sum $\Sigma_{i=1}^4 N_i(T)$ is less than the total number of created pairs. This points to an interesting dual role that is played by the nuclear field. On the one hand, its presence enhances the pair creation rate by providing bound states into which the created electrons can be captured. This seems to be the predominant mechanism for the antinode region of α close to π. On the other hand, for small α, there is a certain fraction of created electrons that are apparently not captured and therefore excite the upper energy continuum states.

Comparing to the data of Fig. 2, which revealed almost no pair-creation in the absence of any nucleus, this suggests a kind of catalytic pair-creation enhancement mechanism. As the interaction with the model nucleus is approximated by a static external force field, there is no backreaction onto the nucleus. The presence of the nucleus can help the created electrons to reach the upper energy continuum states. This mechanism might be similar to the fact that (in the nonrelativistic limit) an electron cannot absorb energy from a plane-wave field, but the presence of a nucleus modifies momentum conservation and therefore "catalyzes" these transitions. In another analogy, if one were to compare the positive and negative energy gap with the energy band gap in a semiconductor, the addition of intermediate levels in the band gap (due to doping) usually increases the change of transition across the band gap as well.

Alternatively, one could also view the bound state as a resonant pathway for the created electrons to reach the upper continuum via some secondary excitation mechanism. Obviously, more detailed studies would be helpful to examine this small α region where the standing waves are forming a high-intensity antinode close to $z = 0$.

C. Variations in the laser frequency ω and in the nuclear size d

While in the prior sequence of simulations the lasers' wavelength $\lambda_L = 2\pi c/\omega_L = 4\pi\lambda$ (associated with $\omega = 0.5\,{\rm mc}^2/\hbar$) and the corresponding node-antinode spacing $\lambda_L/2$ was larger than the spatial extension of the bound states ($2d < \lambda_L/2$; see Fig. 3), we might expect that the anomalous α-scaling of the final yield (due the vacuum state dressing) might be reversed if this relationship is changed such that several nodes and antinodes would "fit" inside the bound states. The two ways to achieve the intuitive behavior $\Gamma(\alpha = 0) > \Gamma(\alpha = \pi)$ are by either increasing ω or by increasing the nuclear spatial range d.

To examine a possible reversed α-dependence of the final yield, we have repeated the numerical simulations leading to Fig. 2 above, however, with a larger laser frequency $\omega = 2.5\,{\rm mc}^2/\hbar$. In Fig. 6(a) we find that now the behavior is indeed reversed, i.e., for the phase $\alpha = 0$ (corresponding to an antinode close to $z = 0$), this time we actually measure the largest pair creation. This behavior is much more intuitive, as the brighter the intensity pattern close to the nucleus is, the larger should be the pair creation.

Alternatively, one can also examine the relationship between the fields' and nucleus' relevant spatial scales by keeping the original laser frequency unchanged at $\omega = 0.5\,{\rm mc}^2/\hbar$, but increasing the nucleus spatial range from $d = 1.95\lambda$ (as in Fig. 4) to $d = 6\lambda$. In Fig. 6(b), we show that we observe again the same intuitive behavior as for $\omega = 2.5\,{\rm mc}^2/\hbar$. Here the effective pair-creation rate (determined from the average slope in the standing-wave region III) is $\Gamma(\alpha = 0) = 5.68$ and only $\Gamma(\alpha = \pi) = 0.22$.

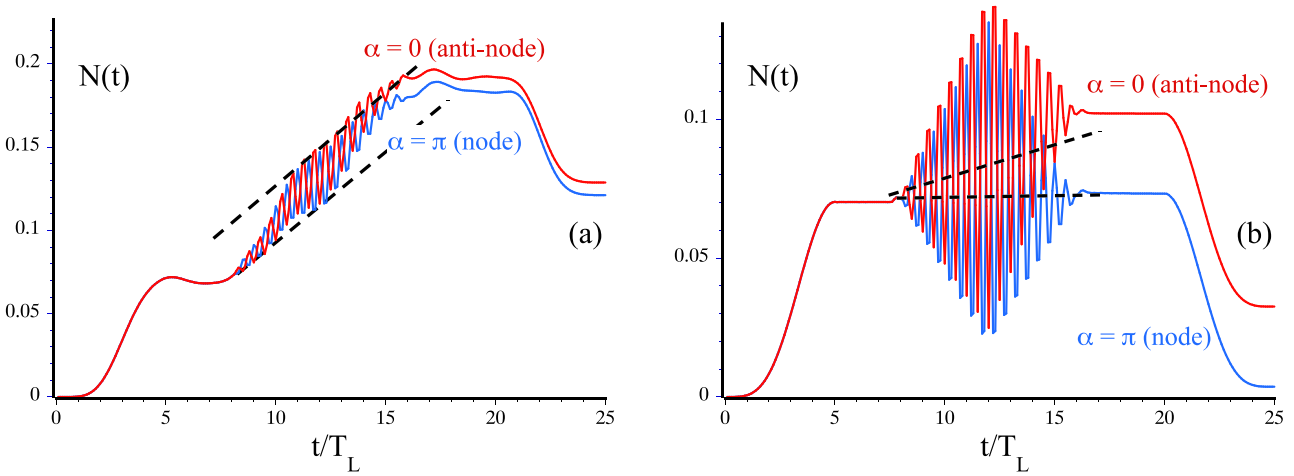

FIG. 6. The time dependence of the total number of created electrons and positrons $N(t)$ for the two phases $\alpha = 0$ and $\alpha = \pi$. (a) High-frequency case with photon energy $\hbar\omega = 2.5\,\mathrm{mc}^2$ and $A_0 = 0.1\,\mathrm{mc}^2/e$ and a narrow potential width $d = 1.95\lambda$ (with $V_0 = -1.85\,\mathrm{mc}^2$ to keep the ground-state energy unchanged at $E_1 = -0.6\,\mathrm{mc}^2$). (b) Low-frequency case, $\hbar\omega = 0.5\,\mathrm{mc}^2$ with $A_0 = 0.1\,\mathrm{mc}^2/e$ but a wider potential width $d = 6\lambda$ (with $V_0 = -1.63\,\mathrm{mc}^2$ to keep the ground-state energy unchanged at $E_1 = -0.6\,\mathrm{mc}^2$). All other parameters as in Figs. 1 and 3. We have included by the straight dashed lines the predicted slopes obtained from Sec. V.

IV. ORIGIN OF THE COUNTERINTUITIVE PHASE DEPENDENCE OF THE GROUND-STATE CAPTURE RATE

In this section, we will suggest that the single-photon coupling matrix element between the relevant initial continuum state $|E\rangle$ and the ground state of the nucleus $|E_1\rangle$ can predict the dependence of the final number of creation particles on the laser phase α and the nucleus spatial range d remarkably well.

As the relatively good match of the total final yield $N(T)$ with $N(T) = \Sigma_i N_i(T)$ (red curve in Fig. 5) suggests, most of the created electrons are captured by the lowest-lying bound states. Therefore, we can neglect the coupling to the positive energy continuum states, i.e., $N(t) = \Sigma_p \Sigma_n |U_{p,n}(t)|^2 + \Sigma_i \Sigma_n |U_{i,n}(t)|^2 \approx \Sigma_i \Sigma_n |U_{i,n}(t)|^2$. Furthermore, as we have seen above, the major contribution is from the ground-state capture, i.e., we can further roughly approximate $N(e^-, t) \approx \Sigma_n |U_{1,n}(t)|^2$. As at early times, the population of the ground state $|U_{1,n}(t)|^2$ is proportional to the magnitude of the transition matrix element $\kappa(\alpha = 0) \equiv \langle E_1 | \cos(kz)\sigma_1 | E\rangle$ for $\alpha = 0$, and to $\kappa(\alpha = \pi) \equiv \langle E_1 | \sin(kz)\sigma_1 | E\rangle$ for $\alpha = \pi$, reflecting the standing-wave pattern with an antinode $A(z, t) \sim \sin(\omega t)\ \cos(kz)$ for the interpulse phase difference $\alpha = 0$ and with a node $A(z, t) \sim \cos(\omega t)\ \sin(kz)$ for $\alpha = \pi$. This means that the origin of the counterintuitive observation $N(T, \alpha = \pi) > N(T, \alpha = 0)$ (Fig. 4) can be possibly tracked back to the α-dependence of the coupling strengths $\kappa(\alpha)$ itself.

In Fig. 7, we have graphed $|\kappa(\alpha, E)|^2$ as a function of the energy E for $\alpha = 0$ and $\alpha = \pi$. The required energy eigenstates to determine $\kappa(\alpha, E)$ were obtained from a numerical diagonalization of the Dirac Hamiltonian $H_0 \equiv c\sigma_1 p + mc^2\sigma_3 + eV(z)$ in a discretized spatial representation.

We see that for photon energy $\hbar\omega = 0.5\,\mathrm{mc}^2$, the anomalous relationship $|\kappa(\alpha = \pi, E)|^2 > |\kappa(\alpha = 0, E)|^2$ is observed quite universally for the entire energy range $E > -1.4\,\mathrm{mc}^2$, while the expected (reversed) inequality is valid only for continuum states much further below the mass gap. It is not immediately clear how the node-based coupling strength $|\kappa(\alpha = \pi)| = |\langle E_1 | \sin(kz)\sigma_1 | E\rangle|$, where the electric field $\sin(kz)$ is rather small close to the ground state $|E_1\rangle$, can actually exceed $|\langle E_1 | \cos(kz)\sigma_1 | E\rangle|$, where the field takes its largest value (antinode) at $z = 0$. This anomaly is certainly not observed for the corresponding coupling to the undressed continuum states $|e\rangle$ to the ground state. Here we

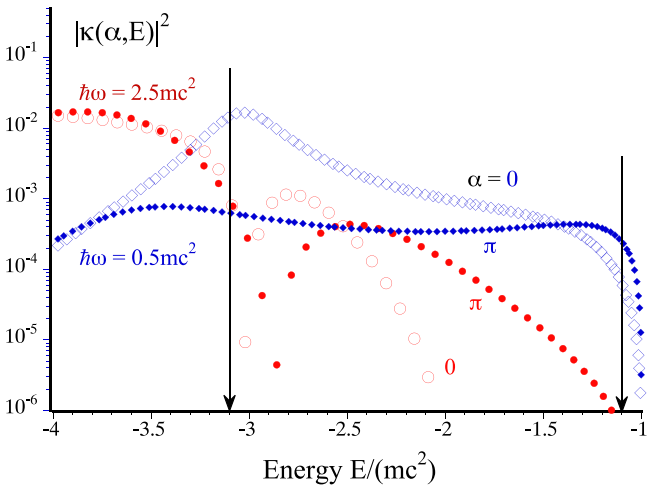

FIG. 7. The scaled part of the transition matrix element to the ground state $|\kappa(\alpha, E)|^2$ as a function of the energy E for the laser phases $\alpha = 0$ (antinode at $z = 0$) and $\alpha = \pi$ (node at $z = 0$). As the eigenstates were obtained by diagonalization of the Dirac Hamiltonian inside a numerical box of $L = 32\lambda_L$, the usual degeneracy among the continuum states is lifted, leading to an energy spacing for $E_c = -1.1\,\mathrm{mc}^2$ of $\Delta E = 3.3 \times 10^{-3}\,\mathrm{mc}^2$. For photon energy $\hbar\omega = 0.5\,\mathrm{mc}^2$, we have $|\kappa(\alpha, E_c)|^2 = 6.5 \times 10^{-5}$ (for $\alpha = 0$) and for $\alpha = \pi$, we have $|\kappa(\alpha, E_c)|^2 = 2.3 \times 10^{-4}$, leading with $A_0 = 0.1\,\mathrm{mc}^2$ to $\Gamma(\alpha = 0) = 11.7$ and $\Gamma(\alpha = \pi) = 43.9$. All four curves are for a potential width and $d = 1.95/c$. The arrows denote the relevant central energies $E_c = -1.1\,\mathrm{mc}^2$ (for $\hbar\omega = 0.5\,\mathrm{mc}^2$) and $E_c = -3.1\,\mathrm{mc}^2$ (for $\hbar\omega = 2.5\,\mathrm{mc}^2$).

find consistently for all energies the more intuitive scaling $|\langle E_1|\cos(kz)\sigma_1|e\rangle| \geqslant |\langle E_1|\sin(kz)\sigma_1|e\rangle|$.

The mathematical reason for the anomalous α-scaling is directly related to the nucleus-induced deformation at $z = 0$ and the resulting shifts of the 2-spinor wave functions as shown in Fig. 3. A closer inspection of the integrand in the spatial integrals $\kappa(\alpha = 0) \sim \langle E_1|\cos(kz)\sigma_1|E\rangle = \int dz \cos(kz)R(z)$ and $\kappa(\alpha = \pi) \sim \int dz \sin(kz)R(z)$, where $R(z) \equiv \Phi_E^{\rm up}(z)^*\Phi_1^{\rm down}(z) + \Phi_E^{\rm down}(z)^*\Phi_1^{\rm up}(z)$ elucidates this. As the state $|E_1\rangle$ has $(+)$ parity, i.e., it has an even upper and odd lower spin component, $\kappa(\alpha = 0)$ is nonzero only for $|E^{(-)}\rangle$. Likewise, $\kappa(\alpha = \pi)$ is nonzero only for the $|E^{(+)}\rangle$ states. For any force-free state $|e\rangle$, the area under the integrand $\cos(kz)\ R(z)$ is larger than under $\sin(kz)R(z)$, as $\sin(kz)R(z)$ vanishes at $z = 0$ where $\phi_1^{\rm up}(z)$ takes its largest value, leading to $|\kappa(\alpha = 0)| > |\kappa(\alpha = \pi)|$. However, this advantage is entirely canceled in the deformed state $|E\rangle$ due to the formation of the "hole" for $R(z)$ at $z = 0$, as was shown in Fig. 3. In other words, the reduction of the integrand due to the cofactor $\sin(kz)$ [compared to $\cos(kz)$] becomes less important. In fact, the different contributions to $R(z)$ of $|E^{(+)}\rangle$ and $|E^{(-)}\rangle$ in the spatial regions outside $z = 0$ can lead to $|\kappa(\alpha = 0)| < |\kappa(\alpha = \pi)|$. The second set of data (photon energy $\hbar\omega = 2.5\,{\rm mc}^2$) shows the reversed behavior. Here the two coupling strengths are comparable for the central energy $E_c = -3.1\,{\rm mc}^2$.

V. ANALYTICAL PAIR-CREATION RATE $\Gamma(\alpha)$ BASED ON AN ESSENTIAL STATE MODEL

The qualitative analysis in Sec. IV and the key relevance of the single parameter κ suggests that, despite the complicated space-time structure of the laser-nucleus interaction zone, the entire pair-creation dynamics can be reduced to a remarkably simple quantum-mechanical-like essential state model, where the initially populated continuum states are coupled to a single bound state. Using several approximations below, we can even derive a semianalytic expression for the total pair-creation rate, which matches well the true observed phase-dependent vacuum decay rate $\Gamma(\alpha)$ obtained from the full quantum field theoretical simulation.

The model considers only the lowest-order single-photon coupling of the continuum state $|E\rangle$ to the ground state $|E_1\rangle$ based on the transition matrix elements $\langle E_1|H_{\rm int}|E\rangle$ of the interaction Hamiltonian $H_{\rm int} \equiv -eA(z, t; \alpha)\sigma_1$. The resulting equations of motion for the two amplitudes of the state $C_E(t)|E\rangle + C_{1,E}(t)|E_1\rangle$ are

$$i\hbar dC_E/dt = EC_E + \langle E_1|H_{\rm int}|E\rangle C_{1,E}, \tag{5.1a}$$

$$i\hbar dC_{1,E}/dt = E_1C_{1,E} + \langle E_1|H_{\rm int}|E\rangle^* C_E, \tag{5.1b}$$

which we need to solve for the ground-state amplitude $C_{1,E}(t)$ with the initial condition $C_{1,E}(t = 0) = 0$ and $C_E(t = 0) = 1$. The total number of created electrons is obtained by summing the contributions to the state $|E_1\rangle$ from all initially occupied continuum states $\Sigma_E|C_{1,E}(t)|^2$. In contrast to the usual essential state formalism often employed for ionization from the ground state in atomic physics, here the state $|E_1\rangle$ is coupled dynamically to only a single continuum state $|E\rangle$. Therefore, the total decay rate of the vacuum state can then be approximated by the time derivative of this sum $\Gamma(\alpha) = -d/dt[\Sigma_E|C_{1,E}(t)|^2]$. This rate $\Gamma(\alpha)$ is rather independent of subsequent higher photon transitions to other bound states. Applying the single-pole, rotating-wave, and Fermi-golden-rule-like approximations, the vacuum's decay rate can be obtained analytically as

$$\Gamma(\alpha) = (\pi/\hbar)A_0^2|k(\alpha, E_c)|^2\rho(E_c). \tag{5.2}$$

Here $\kappa(\alpha, E) \equiv \langle E_1|\cos(kz - \alpha/2)\sigma_1|E\rangle$ is the (scaled) time-independent part of $\langle E_1|H_{\rm int}|E\rangle$, and $\rho(E) \equiv 1/\Delta E$ is the inverse mode spacing evaluated at the specific "resonant" continuum energy $E_c \equiv E_1 - \hbar\omega$.

To test the accuracy of the analytical prediction of Eq. (5.2), we have approximated the growth regions III in the exact data presented in Figs. 4 and 6 by straight lines $N_{\rm tot}(t) = \Gamma(\alpha)t + b(\alpha)$. We have read off the numerical values of the effective slopes and found $\Gamma(\alpha = 0) = 10.2$ [11.3] and $\Gamma(\alpha = \pi) = 35.06$ [44.3] for the data in Fig. 4, $\Gamma(\alpha = 0) = 111.5$ [83.2] and $\Gamma(\alpha = \pi) = 100.5$ [81.1] for Fig. 6(a), and finally $\Gamma(\alpha = 0) = 5.68$ [3.56] and $\Gamma(\alpha = \pi) = 0.22$ [0.187] for the simulations in Fig. 6(b). For comparison with the approximate theory, we have included in the square brackets after each numerical rate the corresponding analytical rates according to Eq. (5.2).

For better visibility, we have also included in Figs. 4 and 6 the predicted slopes according Eq. (5.2) by the straight lines. To have a single quality estimator for the accuracy of the predicted analytical rates, we have also computed the percentage error for each of the six rates shown above, defined as $|\Gamma_{\rm approximate}(\alpha) - \Gamma_{\rm exact}(\alpha)|/\Gamma_{\rm exact}(\alpha)$. The average error amounted to about 22%. The qualitative match of the phase-dependent vacuum decay rate $\Gamma(\alpha)$ with the numerical data suggests that, despite the remarkable simplicity of the model description and its approximations, it can indeed capture the main qualitative features of the irreversible growth part of the electron yield. It can predict both the anomalous behavior $\Gamma(\alpha = 0) < \Gamma(\alpha = \pi)$ as well as the intuitive behavior $\Gamma(\alpha = 0) > \Gamma(\alpha = \pi)$ correctly depending on the laser phase α.

VI. GENERALIZATION TO MULTIPHOTON TRANSITIONS AND EXPERIMENTAL CONSIDERATIONS

Although neither the fields of the laser nor that of the nucleus are required to be of supercritical strength, a direct experimental verification of this effect might still be outside the presently available parameters in the laboratories [72,73]. For example, in order to be sufficiently close to the mass gap energy, we chose a ground-state energy of –0.6 $\rm mc^2$ (0.3 MeV above the negative energy continuum), which might be difficult to realize with a stable nucleus with an atomic number Z close to the inverse of the fine-structure constant. For simplicity, we also examined only the one-photon coupling from the vacuum associated with a photon energy of 0.5 $\rm mc^2$ (0.25 MeV). If we consider, for example, the current energy range of an x-ray free-electron laser such as the one at SLAC's Linear Coherent Light Source, which emits photons in the range 200 eV–11 keV (with a possible future upgrade to 25 keV), then our model would need to be extended to allow for 10-photon transitions.

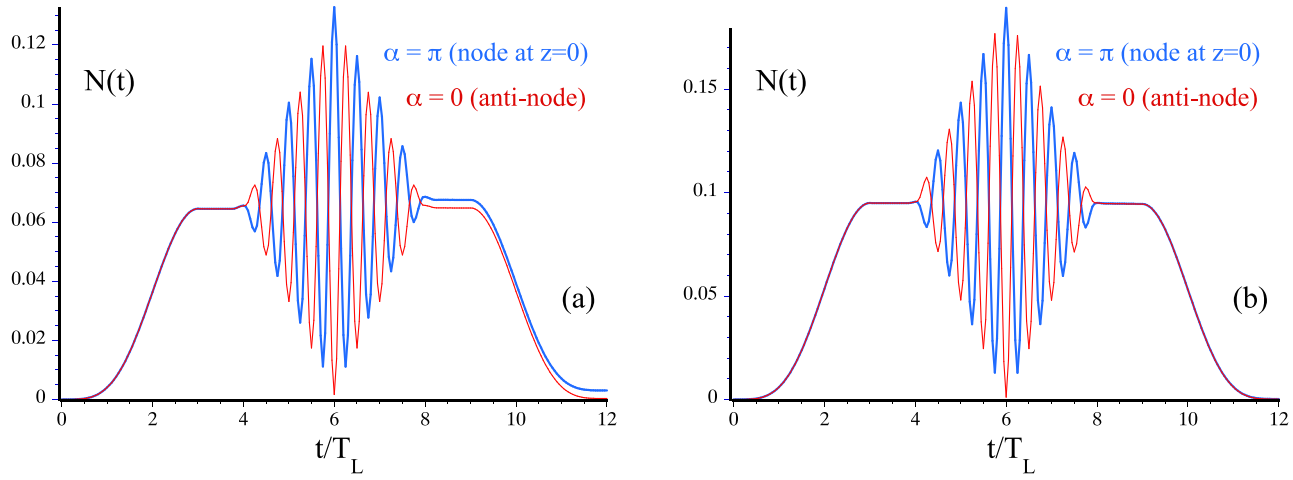

FIG. 8. The time dependence of the total number of created electrons and positrons $N(t)$ for the two phases $\alpha = 0$ and $\alpha = \pi$ in the low-frequency multiphoton regime. (a) Two-photon regime with $\hbar\omega = 0.25\,\mathrm{mc}^2$ (with $A_0 = 0.1\,\mathrm{mc}^2/e$, $z_0 = 6\lambda_L$, $d_L = 2\lambda_L$, $w_L = 0.1\lambda$), leading to $N(T) = 0.000\,31$ for $\alpha = 0$ and $N(T) = 0.003\,04$ for $\alpha = \pi$. Other parameters are as follows: $L = 16\lambda_L$, $V_0 = -1.63c^2$, $w = 0.3\lambda$, and $d = 6\lambda$, with $\lambda_L = 25.12\lambda$. (b) Three-photon regime with $\hbar\omega = 0.167\,\mathrm{mc}^2$ (with $A_0 = 0.1\,\mathrm{mc}^2/e$, $z_0 = 6\lambda_L$, $d_L = 2\lambda_L$, $w_L = 0.1\lambda$) leading to $N(T) = 0.000\,14$ for $\alpha = 0$ and $N(T) = 0.000\,23$ for $\alpha = \pi$. Other parameters are as follows: $L = 16\lambda_L$, $V_0 = -1.63c^2$, $w = 0.3\lambda$, and $d = 6\lambda$, with $\lambda_L = 37.60\lambda$.

The key question that therefore naturally arises is whether the nucleus-induced dressing of the continuum state and the resulting counterintuitive scaling behavior of the pair-creation yield as a function of the phase α can also be observed in the lower-frequency limit, where the absorption of more than one photon is required for pair creation and the resulting electron capture. The answer to this important question is encouraging, as can be shown by simple arguments based on standard perturbation theory in the interaction picture.

For the one-photon coupling, the lowest-order nonvanishing term of the Dyson expansion of the time-evolution operator is usually given by $U_1 \equiv \langle E_1| \int_0^t d\tau \exp[-i(E - E_1)\tau] H_{\mathrm{int}}(\tau)|E\rangle$, whose magnitude for $H_{\mathrm{int}} = -e\,A(z,t;\alpha)\sigma_1$ is, of course, directly proportional to $|\kappa(\alpha, E)|$, as discussed above. Here the temporal integration leads to the well-known resonant energy denominators $E - E_1 - \hbar\omega$. However, the leading term for the two-photon resonance is proportional to the more complicated expression $U_2 \equiv \langle E_1| \int_0^t d\tau [iE_1\tau] H_{\mathrm{int}}(\tau) \exp[-iH_0\tau] \int_0^\tau d\nu \exp[iH_0\nu] H_{\mathrm{int}}(\nu) \exp[-iE\nu]|E\rangle$. Here the relevant resonant energy denominator is $E - E_1 - 2\hbar\omega$. If we insert the unit operator, given by $|E_1\rangle\langle E_1| + \int dE'|E'\rangle\langle E'|$, we find that U_2 can be decomposed into products of factors, where one factor is again proportional to U_1. This suggests that the functional form of the transition element $\kappa(\alpha, E)$ might also be relevant for two- and even higher photon pair-creation processes.

To test this conjecture, we have repeated our simulations in Fig. 8 for the smaller frequency $\omega = 0.25\,\mathrm{mc}^2/\hbar$ (two-photon absorption required) and $\omega = 0.167\,\mathrm{mc}^2/\hbar$ (three-photon absorption required).

We find for the two-photon case again the anomalous behavior due to the modifications of the vacuum state by the binding potential. However, while the anomalous behavior is still present for the three-photon case, it is much weaker. On the one hand, the corresponding larger wavelength for $\omega = 0.167\,\mathrm{mc}^2/\hbar$ leads to a larger spacing between the nodes and antinodes, which by itself would predict a larger contrast between the impacts of the phases $\alpha = 0$ and $\alpha = \pi$. On the other hand, other processes seem to dominate and wash out these differences. Obviously, more systematic studies are required to be able to make quantitative predictions for our present experimentally available laser parameters.

VII. SUMMARY AND OUTLOOK

By examining the pair-creation process triggered by two colliding fields in the presence of a nuclear binding potential that can capture the created electrons, we have found that the phase relationship between the two fields can be used to control not only the total yield of the created electron positron pairs, but also which specific bound states of the nuclear force field can capture the created electrons. Using a remarkably simple essential state model based on only two coupled states, it is possible to derive approximate but semianalytical expressions for the phase dependence of the vacuum decay rate.

To make our simulations computationally feasible required numerous approximations, which unfortunately make a quantitative and reliable experimental prediction quite challenging. Naturally, there are many questions that motivate important further studies. For example, the restriction to only one spatial dimension cannot represent the transverse character of a true electromagnetic field or its magnetic field component. As we critically examined in Sec. VI, our choice of the nuclear potential was also chosen for numerical and interpretational convenience. However, on the more optimistic side, the very fact that the analytical essential state theory matched the actual numerical data is encouraging. One can be hopeful that a similarly constructed quasianalytical theory based on only the essential states could be equally valuable when derived for a real nuclear field in a fully three-dimensional environment.

For example, there is no reason why the set of our approximations (rotating-wave approximation, single-pole approximation, and Fermi-golden-rule-like restrictions to integral kernels) might not be equally valid when applied to a more real system. At the moment we certainly do not see any principal obstacle, except that the accuracy of these new theories could not be so easily compared directly with *ab initio* model simulations, as was possible for our simplified model system.

Another direction of future research work is motivated by the need for a better understanding of the purely electronic capture dynamics associated with the superposition of the excited states. Here it might be of interest to examine the interaction and coherence properties of already captured electrons with those that are created later.

For conceptual simplicity, we focused on identical laser frequencies for both beams of identical temporal and spatial profiles. Recently, fascinating new phenomena such as novel electron and positron momentum shift mechanisms were predicted [65] for temporally overlapping but spatially homogeneous electric fields of different frequencies even in the absence of any nuclear field. We expect that similarly new effects could be discovered if more parameters are varied in our geometry.

A three-dimensional setting would also permit us to weaken our constraint of two perfectly collinear fields as the scattering angle of both beams and their mutual polarization directions could be varied. While in our simulations we have focused exclusively on the electronic features, it might also be interesting to examine the impact of the choice for the two-beam phase on the momentum distribution of the simultaneously created positrons. In our studies, we have focused on the total particle yield as a main diagnostic of the pair-creation process, but examining also the properties of the electronic and positronic spatial distributions can provide further insight into the detailed mechanisms. For recent progress in space-time-resolved studies of the birth process of electron positron pairs inside a very simple temporally homogeneous field, see [74,75].

Due to computational simplicity, we have focused on ultrashort pulses such that the maximum occupation number of the bound states stayed less than 15%. However, for longer interaction times we would expect interesting new multistate Rabi oscillations, once the bound states get fully occupied and also possibly depleted again. The possibility of these Rabi oscillations was examined in recent studies [76], however here the external field was assumed to be spatially homogeneous.

ACKNOWLEDGMENTS

We acknowledge several helpful discussions with Dr. D. D. Su. This work has been supported by the U.S. National Science Foundation (PHY-2106585), the national key R&D program (2018YFA0404802), and the NSFC (11974419) of China.

[1] S. Weinberg, *The Quantum Theory of Fields*, Vol. 1: Foundations (Cambridge University Press, New York, 1995).

[2] P. W. Milonni, *The Quantum Vacuum: An Introduction to Quantum Electrodynamics* (Academic, Boston, 2013).

[3] M. E. Peskin and D. V. Schroeder, *An Introduction to Quantum Field Theory* (CRC, Boca Raton, FL, 1995).

[4] H. B. G. Casimir, On the attraction between two perfectly conducting plates, Proc. K. Ned. Akad. Wet. **51**, 793 (1948).

[5] L. S. Brown, R. N. Cahn, and L. D. McLerran, Vacuum polarization in a strong Coulomb field. I. Induced point charge, Phys. Rev. D **12**, 581 (1975).

[6] For experimental work on the Casimir effect, see G. Bressi, G. Carugno, R. Onofrio, and G. Ruoso, Measurement of the Casimir Force between Parallel Metallic Surfaces, Phys. Rev. Lett. **88**, 041804 (2002).

[7] S. de Man, K. Heeck, R. J. Wijngaarden, and D. Iannuzzi, Halving the Casimir Force with Conductive Oxides, Phys. Rev. Lett. **103**, 040402 (2009).

[8] J. H. Hubbell, Electron–positron pair production by photons: A historical overview, Rad. Phys. and Chem. **75**, 614 (2006).

[9] A. Di Piazza, C. Müller, K. Z. Hatsagortsyan, and C. H. Keitel, Extremely high-intensity laser interactions with fundamental quantum systems, Rev. Mod. Phys. **84**, 1177 (2012).

[10] R. Ruffini, G. Vereshchagin, and S.-S. Xue, Electron–positron pairs in physics and astrophysics: From heavy nuclei to black holes, Phys. Rep. **487**, 1 (2010).

[11] For an excellent review of the recent theoretical and experimental activities in strong field QED, see the abstracts to the ExHilp 2019 conference at Stanford. See http://web.stanford.edu/group/pulse_institute/exhilp.

[12] P. Schlüter, G. Soff, and W. Greiner, Pair creation by internal conversion, Phys. Rep. **75**, 327 (1981).

[13] W. Greiner, B. Müller, and J. Rafelski, *Quantum Electrodynamics of Strong Fields* (Springer, Berlin, 1985).

[14] K. A. Bertulani and G. Baur, Electromagnetic processes in relativistic heavy ion collisions, Phys. Rep. **163**, 299 (1988).

[15] J. Eichler, Theory of relativistic ion-atom collisions, Phys. Rep. **193**, 165 (1990).

[16] G. Baur, K. Hencken, and D. Trautman, Electron–positron pair production in ultrarelativistic heavy ion collisions, Phys. Rep. **453**, 1 (2007).

[17] F. Sauter, On the behavior of an electron in a homogeneous electric field in Dirac's relativistic theory, Z. Phys. **69**, 742 (1931).

[18] J. Schwinger, On gauge invariance and vacuum polarization, Phys. Rev. **82**, 664 (1951).

[19] F. Gelis and N. Tanji, Schwinger mechanism revisited, Prog. Part. Nucl. Phys. **87**, 1 (2016).

[20] J. Thiel, A. Bunker, K. Momberger, N. Grün, and W. Scheid, Electron-positron pair creation with capture and ionization in relativistic heavy-ion collisions by the finite-difference method, Phys. Rev. A **46**, 2607 (1992).

[21] C. Müller, A. B. Voitkiv, and N. Grün, Nonlinear Bound-Free Pair Creation in the Strong Electromagnetic Fields of a Heavy Nucleus and an Intense X-ray Laser, Phys. Rev. Lett. **91**, 223601 (2003).

[22] D. D. Su, Y. T. Li, Q. Su, and R. Grobe, Laser-induced level shifts and splittings in multiphoton pair creation, Phys. Rev. D **103**, 074513 (2021).

[23] J. W. Motz, H. A. Olsen, and H. W. Koch, Pair production by photons, Rev. Mod. Phys. **41**, 581 (1969).

[24] Y. I. Salamin, S. X. Hu, K. Z. Hatsagortsyan, and C. H. Keitel, Relativistic high-power laser–matter interactions, Phys. Rep. **427**, 41 (2006).

[25] B. S. Xie, Z. L. Li, and S. Tang, Electron-positron pair production in ultrastrong laser fields, Matter Radiat. Extremes **2**, 225 (2017).

[26] H. Hu, Seed and vacuum pair production in strong laser field, Cont. Phys. **61**, 12 (2020).

[27] D. L. Burke *et al.*, Positron Production in Multiphoton Light-by-Light Scattering, Phys. Rev. Lett. **79**, 1626 (1997).

[28] See https://eli-laser.eu; I. C. E. Turcu *et al.*, Rom. Rep. Phys. **68**, S145 (2016).

[29] See https://corels.ibs.re.kr.

[30] For a nice project overview of the E-320 collaboration at FACET-II (https://facet.slac.stanford.edu) see the conference slides by S. Meuren, https://conf.slac.stanford.edu/facet-2-2019/sites/facet-2-2019.conf.slac.stanford.edu/files/basic-page-docs/sfqed_2019.pdf, presented at the FACET-II Science Workshop 2019 at SLAC.

[31] C. H. Keitel, A. Di Piazza, G. G. Paulus, T. Stoehlker, E. L. Clark, S. Mangles, Z. Najmudin, K. Krushelnick, J. Schreiber, M. Borghesi, B. Dromey, M. Geissler, D. Riley, G. Sarri, and M. Zepf, Photo-induced pair production and strong field QED on Gemini, arXiv:2103.06059.

[32] See http://www.hibef.eu; H. Abramowicz *et al.*, Conceptual design report for the LUXE experiment, Eur. Phys. J.: Spec. Top. **230**, 2445 (2021).

[33] As an example for a work where the spatiotemporal dependence of two counterpropagating laser fields and their magnetic components were explicitly taken into account, see M. Ruf, G. R. Mocken, C. Müller, K. Z. Hatsagortsyan, and C. H. Keitel, Pair Production in Laser Fields Oscillating in Space and Time, Phys. Rev. Lett. **102**, 080402 (2009).

[34] E. Brezin and C. Itzykson, Pair production in vacuum by an alternating field, Phys. Rev. D **2**, 1191 (1970).

[35] N. B. Narozhnyi and A. I. Nikishov, Simplest processes in the pair-creating electric field, Yad. Fiz. **11**, 1072 (1970).

[36] V. S. Popov, Pair production in a variable external field (quasiclassical approximation), Zh. Eksp. Teor. Fiz. **61**, 1334 (1971) [Sov. Phys. JETP. **34**, 709 (1972)].

[37] A. A. Grib, V. M. Mostepanenko, and V. M. Frolov, Particle creation from vacuum by a homogeneous electric field in the canonical formalism, Theor. Math. Phys. **13**, 1207 (1972).

[38] V. G. Bagrov, D. M. Gitman, and Sh. M. Shvartsman, Concerning the production of electron-positron pairs from vacuum, Zh. Eksp. Teor. Fiz. **68**, 392 (1975) [Sov. Phys. JETP **41**, 191 (1975)].

[39] S. S. Bulanov, V. D. Mur, N. B. Narozhny, J. Nees, and V. S. Popov, Multiple Colliding Electromagnetic Pulses: A Way to Lower the Threshold of E^+E^- Pair Production from Vacuum, Phys. Rev. Lett. **104**, 220404 (2010).

[40] C. Kohlfürst, M. Mitter, G. von Winckel, F. Hebenstreit, and R. Alkofer, Optimizing the pulse shape for Schwinger pair production, Phys. Rev. D **88**, 045028 (2013).

[41] F. Hebenstreit and F. Fillion-Gourdeau, Optimization of Schwinger pair production in colliding laser pulses, Phys. Lett. B **739**, 189 (2014).

[42] S. S. Dong, M. Chen, Q. Su, and R. Grobe, Optimization of spatially localized electric fields for electron-positron pair creation, Phys. Rev. A **96**, 032120 (2017).

[43] J. Unger, S. Dong, Q. Su, and R. Grobe, Optimal supercritical potentials for the electron-positron pair-creation rate, Phys. Rev. A **100**, 012518 (2019).

[44] J. Eichler and T. Stöhlker, Radiative electron capture in relativistic ion–atom collisions and the photoelectric effect in hydrogen-like high-Z systems, Phys. Rep. **439**, 1 (2007).

[45] For a recent extensive review, see A. Fedotov, A. Ilderton, F. Karbstein, B. King, D. Seipt, H. Taya, and G. Torgrimsson, Advances in QED with intense background fields, Phys. Rep. **1010**, 1 (2023).

[46] C. Müller, A. B. Voitkiv, and N. Grün, Differential rates for multiphoton pair production by an ultrarelativistic nucleus colliding with an intense laser beam, Phys. Rev. A **67**, 063407 (2003).

[47] E. Lötstedt, U. D. Jentschura, and C. H. Keitel, Coulomb-field-induced conversion of a high-energy photon into a pair assisted by a counterpropagating laser beam, New J. Phys. **11**, 013054 (2009).

[48] A. Di Piazza, E. Lötstedt, A. I. Milstein, and C. H. Keitel, Coulomb-field-induced conversion of a high-energy photon into a pair assisted by a counterpropagating laser beam, Phys. Rev. A **81**, 062122 (2010).

[49] K. Krajewska and J. Z. Kaminski, Recoil effects in multiphoton electron-positron pair creation, Phys. Rev. A **82**, 013420 (2010).

[50] S. Augustin and C. Müller, Nonperturbative Bethe–Heitler pair creation in combined high- and low-frequency laser fields, Phys. Lett. B **737**, 114 (2014).

[51] B. Hafizi, D. F. Gordon, and D. Kaganovich, Pair Creation with Strong Laser Fields, Compton Scale X Rays, and Heavy Nuclei, Phys. Rev. Lett. **122**, 233201 (2019).

[52] H. A. Bethe and W. Heitler, On the stopping of fast particles and on the creation of positive electrons, Proc. R. Soc. A **146**, 83 (1934).

[53] N. R. Larin, V. V. Dubov, and S. P. Roshchupkin, Resonant photoproduction of high-energy electron-positron pairs in the field of a nucleus and a weak electromagnetic wave, Phys. Rev. A **100**, 052502 (2019).

[54] N. R. Larin, V. V. Dubov, and S. P. Roshchupkin, Resonant production of electron-positron pairs by a hard gamma-ray on a nucleus in an external electromagnetic field, Mod. Phys. Lett. A **35**, 2040025 (2020).

[55] N. R. Larin, S. P. Roshchupkin, and V. V. Dubov, Resonant effects in a photoproduction of ultrarelativistic electron-positron pairs on a nucleus in the field of the X-ray pulsar, Universe **6**, 141 (2020).

[56] S. P. Roshchupkin, N. R. Larin, and V. V. Dubov, Resonant effect of the ultrarelativistic electron–positron pair production by gamma quanta in the field of a nucleus and a pulsed light wave, Laser Phys. **31**, 045301 (2021).

[57] C. K. Li, D. D. Su, Y. J. Li, Q. Su, and R. Grobe, Probing the spatial structure of the Dirac vacuum via phase-controlled colliding laser pulses, Eur. Phys. Lett. **141**, 55001 (2023).

[58] For a review, see T. Cheng, Q. Su, and R. Grobe, Introductory review on quantum field theory with space-time resolution, Cont. Phys. **51**, 315 (2010).

[59] C. C. Gerry, Q. Su, and R. Grobe, Timing of pair-production in time-dependent force fields, Phys. Rev. A **74**, 044103 (2006).

[60] P. Krekora, Q. Su, and R. Grobe, Interpretational difficulties in quantum field theory, Phys. Rev. A **73**, 022114 (2006).

[61] H. Taya, H. Fujii, and K. Itahura, Finite pulse effects on e^+e^- pair creation from strong electric fields, Phys. Rev. D **90**, 014039 (2014).

[62] R. Dabrowski and G. V. Dunne, Superadiabatic particle number in Schwinger and de Sitter particle production, Phys. Rev. D **90**, 025021 (2014).

[63] R. Dabrowski and G. V. Dunne, On the time dependence of adiabatic particle number, Phys. Rev. D **94**, 065005 (2016).

[64] A. Ilderton, Physics of adiabatic particle number in the Schwinger effect, Phys. Rev. D **105**, 016021 (2022).

[65] N. Folkerts, J. Putzer, S. Villalba-Chávez, and C. Müller, Electron-positron-pair creation in the superposition of two oscillating electric-field pulses with largely different frequency, duration, and relative positioning, Phys. Rev. A **107**, 052210 (2023).

[66] M. Diez, R. Alkofer, and C. Kohlfürst, Identifying time scales in particle production from fields, Phys. Lett. B **844**, 138063 (2023).

[67] V. B. Berestetskii, E. M. Lifshitz, and L. P. Pitaevskii, *Relativistic Quantum Theory* (Pergamon, Surrey, UK, 1971).

[68] A. Di Piazza, Ultrarelativistic Electron States in a General Background Electromagnetic Field, Phys. Rev. Lett. **113**, 040402 (2014).

[69] A. Di Piazza, Analytical tools for investigating strong-field QED processes in tightly focused laser fields, Phys. Rev. A **91**, 042118 (2015).

[70] A. Di Piazza, Nonlinear Breit-Wheeler Pair Production in a Tightly Focused Laser Beam, Phys. Rev. Lett. **117**, 213201 (2016).

[71] Q. Z. Lv, S. Dong, Y. T. Li, Z. M. Sheng, Q. Su, and R. Grobe, Role of the spatial inhomogeneity on the laser-induced vacuum decay, Phys. Rev. A **97**, 022515 (2018).

[72] C. N. Danson, C. Haefner, J. Bromage *et al.*, Petawatt and exawatt lasers worldwide, in *High Power Laser Science and Engineering* (Cambridge University Press, 2019).

[73] For the presently largest accessible laser intensity, see J. W. Yoon, Y. G. Kim, I. W. Choi, J. H. Sung, H. W. Lee, S. K. Lee, and C. H. Nam, Realization of laser intensity over 10^{23} W/cm^2, Optica **8**, 630 (2021).

[74] C. Gong, J. Bryan, Q. Su, and R. Grobe, Machine learning techniques in the examination of the electron-positron pair creation process, J. Opt. Soc. Am. B **38**, 3582 (2021).

[75] C. Gong, Q. Su, and R. Grobe, Birth process of electron-positron pairs inside supercritical fields, Eur. Phys. Lett. **141**, 65001 (2023).

[76] D. D. Su, C. K. Li, Q. Su, and R. Grobe, Control of the laser-induced vacuum decay by electronic phases, Phys. Rev. A **105**, 053114 (2022).